Charge Collective Modes in Correlated Electron Systems: Plasmons Beyond the Random Phase Approximation

Loïc Philoxene,[1] Vu Hung Dao,[1] and Raymond Frésard[1]

[1]*Normandie Université, ENSICAEN, UNICAEN, CNRS, CRISMAT, 14000 Caen, France*

(Dated: March 27, 2024)

Elucidating the impact of strong electronic interactions on the collective excitations of metallic systems has been of longstanding interest, mainly due to the inadequacy of the random phase approximation (RPA) in the strongly correlated regime. Here, we adopt our newly developed radial Kotliar and Ruckenstein slave boson representation to analyze the charge excitation spectrum of a Hubbard model, extended with long range interactions. Working on the face centered cubic lattice, at half filling, and in different coupling regimes ranging from uncorrelated to the metal-to-insulator transition, we compare our results to conventional RPA as a benchmark. We focus on the influence of the local and long range couplings on the particle-hole excitation continuum and the plasmon and upper Hubbard band collective modes. Beyond the weak coupling regime, we find numerous quantitative and even qualitative discrepancies between our method and standard RPA. Our work thus deepens our understanding of charge collective modes in correlated systems, and lays the foundations for future studies of realistic materials.

Introduction.— In their seminal series of papers, Pines and Bohm pioneered the study of collective modes arising in dynamical autocorrelation functions of the electron gas by introducing the random phase approximation (RPA) [1–3]. Focusing on density fluctuations, they argued that their spectra may be split into two components: i) an incoherent one associated with the random thermal motion of the individual electrons, and ii) a plasma oscillation mode. Having a classical analogue, the latter may be explained in simple terms, and is broadly documented [4–6]. Nevertheless, quantum corrections to this classical picture were recently addressed [7]. Furthermore, a series of applications backing on its existence have been put forward, ranging from nanophotonics [8–21], to energy conversion [22–26], and even cancer treatment [27–31].

Since its introduction, it has been established that the RPA remains sensible in the weak coupling regime only, and that it becomes unreliable as soon as the coupling strength becomes intermediate. Nevertheless, it may still be applied as a flexible tool in the thermodynamic limit, and it indeed remains broadly used, especially within quantum chemistry codes [32–34]. Besides, a series of calculations on model systems demonstrated qualitative failures of the approximation, especially in the context of the celebrated one band Hubbard model. In fact, key quantum collective phenomena entailed by the model, for example the signature of the upper Hubbard band, are missing in the charge excitation spectra when computed within the RPA. Multiple frameworks that try to overcome some of these shortcomings, and recover some of the missing features, have thus been proposed [35–40].

A broadly used approach to tackle correlated electrons is provided by Kotliar and Ruckenstein's slave boson (KRSB) representation. This versatile tool may be applied to a series of microscopic models, such as the Hubbard model [41] and its extensions [42–44]. It consists in introducing a doublet of pseudofermions, along with four bosons, that generate the Fock space on each lattice site. In the functional integral formulation, this results in a Lagrangian that is bi-linear in the fermionic fields, although no Hubbard-Stratonovich decoupling is performed, thereby allowing for a description of electronic interactions at arbitrary coupling strengths. The reliability of the KRSB representation to the Hubbard model and its extensions has already been extensively discussed (see, e.g., Paragraph II.C.1 in Ref. [45] and references therein). A recent study also put forward quantitative agreement between the charge and spin structure factors computed in KRSB and resonant inelastic x-ray scattering data [44]. Within this representation, calculations are amenable to the thermodynamic limit as well. In the saddle-point approximation, it is equivalent to the Gutzwiller approximation and is consistently capable of describing a Mott metal-to-insulator transition in the form of the Brinkman-Rice transition. It therefore does not suffer from a weak coupling limitation. The resulting low energy spectra qualitatively differ from the RPA results, however [46]. They generically comprise a continuum, a zero-sound collective mode lying slightly above this continuum, and a signature of the upper Hubbard band in the form of a mode that disperses about $\omega \sim U$ in the strong coupling regime. Below, we refer to the latter as the upper Hubbard band mode. This mode may, in the intermediate coupling regime, hybridize with the zero-sound one [46].

In the past twenty years, the extended Hubbard model, entailing non-local density-density interactions, has seen an upsurge of interest [45, 47–56] (see also [57] and references therein for a better overview). It has also been studied early on within the KRSB representation, and phase diagrams have been computed [42]. Below, we apply the radial gauge of the KRSB representation [58], in which the non-local interaction is also rewritten as

a bi-linear term in the boson fields, which allows for a systematic evaluation of long range correlations between density fluctuations. This formalism has recently been validated through exact calculations [59, 60].

The purpose of the present Letter is to compute the experimentally accessible energy loss spectrum of the extended Hubbard model, via the calculation of the dynamical dielectric function, which itself depends on the charge autocorrelation function. Special focus is made on the interplay of the plasmon mode (driven by the non-local Coulomb interaction), the upper Hubbard band (driven by the local interaction), and the low energy particle-hole excitation continuum.

Model and methods.— The Hamiltonian for the Hubbard model, extended by a long range Coulomb interaction, may be written as

$$\mathcal{H} = \sum_{i\neq j,\sigma} t_{ij}\left(c^\dagger_{\sigma,i}c_{\sigma,j} + \text{h.c.}\right) + U\sum_i n_{\uparrow,i}n_{\downarrow,i} + \frac{1}{2}\sum_{i\neq j} V_{ij}\left(2-\sum_\sigma n_{\sigma,i}\right)\left(2-\sum_\sigma n_{\sigma,j}\right), \quad (1)$$

where $c_{i,\sigma}$ ($\sigma = \uparrow,\downarrow$) is the canonical electron annihilation operator, $n_{i,\sigma}$ is the associated electron number operator, $t_{ij} = -t$ if i and j are nearest neighbors, and $t_{ij} = 0$ otherwise. Here, t is the hopping amplitude, U is the Hubbard coupling, and $V_{ij} = Va/|\mathbf{r}_i - \mathbf{r}_j|$ is the non-local Coulomb interaction, where a is the lattice spacing, and V is an effective coupling parameter. Note that in the last term, the interaction couples the hole densities $2-n$ instead of the electron densities n. This choice of representation for the long range interaction has been made for later convenience, and is equivalent to the representation in terms of electron densities, as it only induces an overall energy shift in the spectrum of $\mathcal{H}$.

We work in the grand canonical ensemble, and employ the radial gauge of the KRSB representation. In this paragraph, we give an outline of the formalism behind this radial KRSB representation, and refer to, for example Ref. [60] for a more detailed discussion. In the original KRSB framework, one introduces a set of four auxiliary bosons e, p_σ, and d (associated to unoccupied, singly occupied with spin projection σ, and doubly occupied atomic states, respectively), as well as a doublet of pseudofermions f_σ at each lattice site. Within the functional integral formalism, the canonical electron fields are mapped to a product of slave boson and pseudofermion fields as

$$c_{\sigma,i}(\tau) \to z_{\sigma,i}(\tau) f_{\sigma,i}(\tau), \quad (2)$$

where the fields $z_{\sigma,i}(\tau)$ are functions of the boson fields (omitting the imaginary-time variable τ),

$$z_{\sigma,i} = e^*_i L_{\sigma,i} R_{\sigma,i}\, p_{\sigma,i} + p^*_{-\sigma,i} L_{\sigma,i} R_{\sigma,i}\, d_i, \quad (3)$$

where

$$L_{\sigma,i} = (1 - p^*_{\sigma,i}p_{\sigma,i} - d^*_i d_i)^{-1/2},$$
$$R_{\sigma,i} = (1 - p^*_{-\sigma,i}p_{-\sigma,i} - e^*_i e_i)^{-1/2}. \quad (4)$$

This representation is invariant under local $\mathrm{U}(1)\times\mathrm{U}(1)\times\mathrm{U}(1)$ gauge transformations, allowing for the phase of three of the boson fields to be gauged away [61–63]. The boson fields deprived of their phase degree of freedom are coined radial slave bosons. Being real-valued, the radial slave boson fields are free from Bose condensation. Their expectation values are generically finite and can be well approximated in the thermodynamic limit via the saddle-point approximation. Corrections to the latter may be obtained when evaluating the Gaussian fluctuations [46], and the correspondence between this more precise evaluation and the time-dependent Gutzwiller approach [64] could recently be achieved—though by means of an extension in the formulation of the latter [65]. Exact results may be obtained for, e.g., a simplified single-impurity Anderson model, the Ising chain, or small correlated clusters [58–60, 66]. After projection onto the physical Hilbert space, the averaged value of the square of any radial slave boson amplitude equals the averaged value of the radial field itself [66]. This allows for a rewriting of the functional integral as a Gaussian integral over the slave boson and pseudofermion fields, even in the presence of non-local interactions [58]. The validity of the radial KRSB representation has been assessed through exact evaluation of the partition function in the atomic limit [59], and most recently for the two-site cluster [60]. Following Ref. [60], we use the radial fields R_e and R_σ corresponding to the squared amplitudes of the fields e and p_σ, respectively, while d is kept complex.

The charge excitation spectrum of the model can be analyzed through the evaluation of the loss function $-\mathrm{Im}[\varepsilon^{-1}(\mathbf{q},\omega)]$, which is experimentally accessible by electron energy loss spectroscopy or resonant inelastic x-ray scattering measurements. To that end, we compute the inverse dynamical dielectric function as

$$\varepsilon^{-1}(\mathbf{q},\omega) = 1 - \left[\frac{U}{2} + V(\mathbf{q})\right]\chi_c(\mathbf{q},\omega), \quad (5)$$

where the charge susceptibility $\chi_c(\mathbf{q},\omega)$ is calculated by taking into account Gaussian fluctuations about the paramagnetic saddle-point solution, and performing the analytical continuation $\mathrm{i}\omega_n \to \omega + \mathrm{i}0^+$ on the density-density correlation function:

$$\begin{aligned}\chi_c(q) &= \langle\delta n(-q)\delta n(q)\rangle \\ &= 4d^2\langle\delta d'(-q)\delta d'(q)\rangle - 2d\langle\delta d'(-q)\delta R_e(q)\rangle \\ &\quad + \langle\delta R_e(-q)\delta R_e(q)\rangle. \end{aligned} \quad (6)$$

where, $q \equiv (\mathbf{q}, \mathrm{i}\omega_n)$, $\omega_n \equiv 2\pi n k_B T$, k_B is the Boltzmann constant, and T is the temperature. Within this

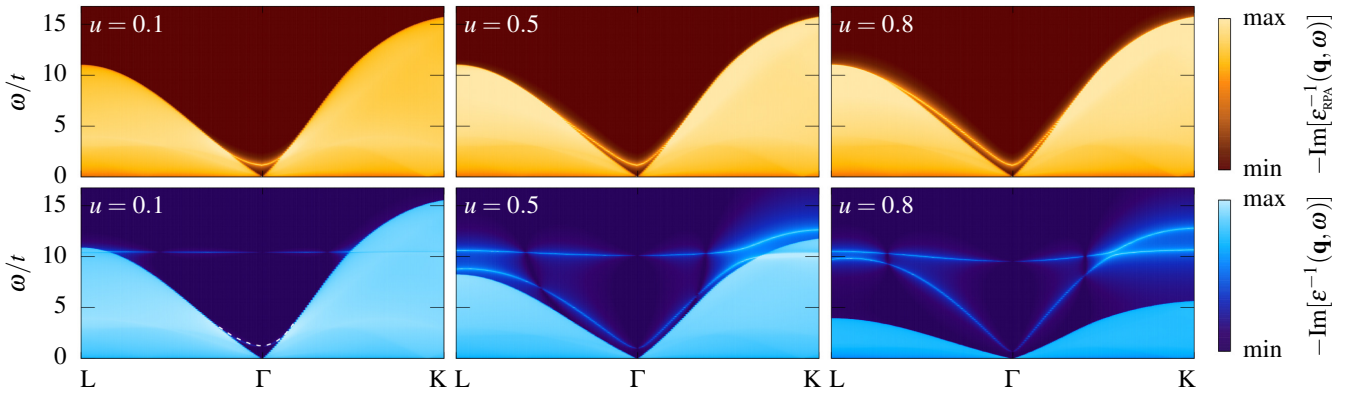

FIG. 1. Zero temperature RPA (top row) and radial KRSB (bottom row) energy loss spectra $-\mathrm{Im}[\varepsilon^{-1}(\mathbf{q},\omega)]$, in dependence on $\mathbf{q}$ along $L-\Gamma-K$. Parameters: $v=0.1$ and $u=0.1$, 0.5, and 0.8, from left to right. The white dashed line in the bottom-left panel helps visualizing the weak plasmon mode.

level of approximation, correlation functions between the boson fields may be suitably computed as Gaussian integrals [46].

The paramagnetic saddle-point of the KRSB representation has already been extensively studied in the literature [41–43, 46, 67]. In radial gauge, the study of the saddle-point remains identical.

In this Letter, we focus on the face centered cubic lattice as a representative example of three dimensional systems, since the simple cubic structure is scarcely realized. In this case, the bare dispersion is $t_{\mathbf{k}} = -4t\left(\cos\frac{k_x}{2}\cos\frac{k_y}{2}+\cos\frac{k_y}{2}\cos\frac{k_z}{2}+\cos\frac{k_z}{2}\cos\frac{k_x}{2}\right)$, where we set $a=1$. As a proof of principle, we consider the half band-filling ($n=1$) case, which hosts the metal-to-insulator transition, thereby allowing us to unravel the impact of strong electron correlations on the loss function. In this context, the critical coupling of the Mott transition is

$$U_c = -8\xi_{\mathbf{0}}, \tag{7}$$

where $\xi_{\mathbf{0}}$ the average bare kinetic energy energy. We find $\xi_{\mathbf{0}} \simeq -2.6t$, yielding $U_c \simeq 21t$, as compared to $16t$ for the simple cubic lattice. In the following, we work in a system of units in which $\hbar = 1$.

Results.— In the standard Hartree-Fock RPA (HF+RPA) framework, the density-density correlation function is computed as a series of particle-hole bubble diagrams for non-interacting electrons, linked with bare interaction vertices $U/2 + V(\mathbf{q})$. Under such approximations, the dynamical dielectric function reads [6]

$$\varepsilon_{\mathrm{RPA}}(\mathbf{q},\omega) = 1 + \left[\frac{U}{2}+V(\mathbf{q})\right]\Pi_0^{(0)}(\mathbf{q},\omega), \tag{8}$$

where $\Pi_0^{(0)}(\mathbf{q},\omega)$ is the Lindhard function for the non-interacting system. Due to its perturbative essence, we cannot expect standard HF+RPA procedure to yield reasonable results in the strong coupling regime (see [46] and Supplemental Material for an assessment of some of the key features missing in the RPA treatment that are incorporated in the Cartesian and radial KRSB formalisms, respectively). However, we use it as a benchmark to highlight strong correlation effects when comparing it with the radial KRSB representation for values of U and/or V approaching U_c. In the following, we use the dimensionless coupling parameters $u = U/U_c$ and $v = V/U_c$.

Let us now address representative examples of the energy loss spectra computed with Eq. (8) and with Eq. (5). We fix the value of $v = 0.1$ and investigate values of $u = 0.1$, 0.5, and 0.8 at half filling. We also focus on values of $\mathbf{q}$ along the representative symmetry lines $L-\Gamma-K$, with $L=(\pi,\pi,\pi)$, $\Gamma=(0,0,0)$, and $K=(\frac{3\pi}{2},\frac{3\pi}{2},0)$, for the wavevector dependence. On the face centered cubic lattice, the nearest neighbor distance is smallest (largest) along the $\Gamma-K$ ($\Gamma-L$) direction. The computed spectra are presented in Fig. 1. They generically comprise a low energy particle-hole excitation continuum. In RPA, this continuum is insensitive to the value of u, and it disperses from $\omega(\Gamma)=0$, up to $\omega(K)\simeq 16t$. In our radial KRSB calculations, however, the continuum strongly depends on the value of u. Indeed, it is gradually narrowed by increasing the Hubbard coupling, with a maximum of its dispersion at $\omega(K)\simeq 16t$ for $u=0.1$, in contrast to $\omega(K)\simeq 6t$, only, for $u=0.8$. This owes to the fact that, at zero temperature, the Lindhard function for the quasiparticles $\Pi_0(\mathbf{q},\omega)$ and the non-interacting Lindhard function $\Pi_0^{(0)}(\mathbf{q},\omega)$ are related via renormalization:

$$\Pi_0(\mathbf{q},\omega) = \frac{1}{z_0^2}\Pi_0^{(0)}\left(\mathbf{q},\frac{\omega}{z_0^2}\right). \tag{9}$$

Here, z_0 is the saddle-point value of the field Eq. (3). We thus explicitly see the decrease of the continuum's

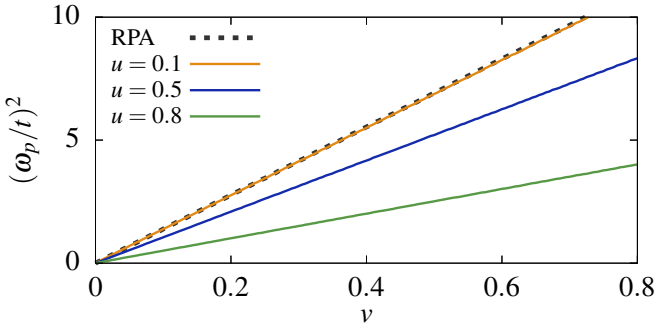

FIG. 2. Square of the plasma frequency ω_p^2 in dependence on the strength of the effective Coulomb coupling v. Parameters: $u = 0.1$, 0.5, and 0.8. The plasma frequency obtained in RPA is also shown.

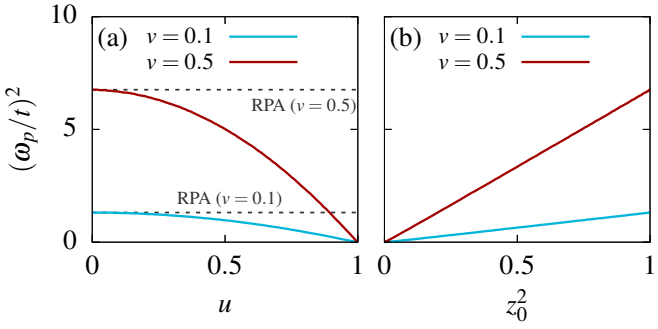

FIG. 3. Square of the radial KRSB plasma frequency ω_p^2, in dependence on (a) the local coupling u, and (b) the quasiparticle residue z_0^2. Parameters: $v = 0.1$ and 0.5. In (a), the RPA plasma frequency is also shown in dashed lines.

bandwidth, as the quasiparticle residue z_0^2 approaches zero when u approaches one [46].

Above this continuum, in RPA, a single collective mode establishes, at large wavelengths. When increasing $\mathbf{q}$, it enters the particle-hole continuum, and thus quickly becomes suppressed by Landau damping. For larger values of u, this collective mode gets overdamped at larger energy and wavevector, especially in the L direction, along which it disperses more. Its gap at $\mathbf{q} = \Gamma$, however, remains unchanged and in fact depends on v, only. This collective mode actually corresponds to plasmon collective excitations. This can be seen by comparing the value of its gap at $\mathbf{q} = \Gamma$ to the plasma frequency predicted by a large wavelength expansion of the dielectric function (see Supplemental Material for a derivation),

$$\omega_p \simeq \sqrt{-\frac{V\xi_{\mathbf{0}}}{6}}. \tag{10}$$

For $v = 0.1$ (i.e. $V = 2.1t$), this yields $\omega_p \simeq t$, which coincides with the gap shown in the top row of Fig. 1. Furthermore, we note that the plasma frequency computed with this expression does not depend on the value of u, which also concurs with our results. In fact, u first enters the dispersion of the plasmon mode as a contribution of order $|\mathbf{q}|^2$. This additionally corroborates the observation that the plasmon mode disperses more for larger values of the Hubbard coupling. In the bottom row of Fig. 1, we see that the radial KRSB spectra possess two well-defined collective modes. Firstly, we observe the plasmon mode, similarly to the RPA. At weak coupling $u = 0.1$, the plasmon collective mode is also present at large wavelengths, only, as it enters the particle-hole continuum at approximately the same values of $\mathbf{q}$ and ω as in RPA. At larger couplings $u = 0.5$ and 0.8, though, the renormalization of the particle-hole continuum, along with the greater dispersion of the plasmon mode induced by u, allows for the latter to remain well-defined in a broader range of wavelengths. From the bottom row of Fig. 1 only the radial KRSB plasma frequency appears to remain almost equal to that observed within the RPA, but this will be analyzed in greater detail below. Secondly, an additional collective mode establishes in the radial KRSB spectra. This mode, with a much larger gap at Γ of about $\omega_{\mathrm{UHB}} \simeq 10t$ for every values of u, corresponds to the aforementioned upper Hubbard band mode. Similarly to the plasmon mode, at weak coupling, it enters the particle-hole continuum at finite $\mathbf{q}$, inside which it quickly decays via Landau damping. It, however, disperses much less than the plasmon mode, with a bandwidth of at most one for $u = 0.8$.

In this two-modes picture, one might expect a level-crossing at finite $\mathbf{q}$ between the two bands, at a given point of the parameter space. Yet, no point of exact degeneracy could be found, but either no-crossing or anticrossings between both modes, as depicted in the center and right panels of the bottom row in Fig. 1. Nonetheless, we observe multiple anticrossings with near-degeneracy, as can be seen for example close to $K/2$ and energies around $\omega \simeq 10t$ for $u = 0.8$. Close to these anticrossings, the upper Hubbard band mode and the plasmon mode strongly hybridize, and the excitations share both characters.

Fig. 2 presents the v dependence of the radial KRSB plasma frequency squared ω_p^2, for values of $u = 0.1$, 0.5, and 0.8. The RPA result is also shown for comparison, and one can see that in the weak coupling regime, the radial KRSB formalism correctly reproduces the RPA plasma frequency, as expected. Another expected property of the square of the plasma frequency is that it should scale with v, as we have $\omega_p^2 \simeq 9.2v$ at weak coupling, which is also realized. However, the deviation of the plasma frequency from this analytical expression is seen to increase with u. This indicates that strong correlation effects, arising when the local coupling becomes sufficiently large, cause a softening of the plasmon mode, by opposition to the RPA picture in which the plasmon mode is affected by the strength of the local interaction at finite wavevectors, only.

The u dependence of the radial KRSB plasma frequency squared is shown in Fig. 3(a), for representative values of $v = 0.1$ and 0.5. The RPA result, for the same values of v, is also presented for comparison. We see that the plasma frequency decreases as the Hubbard coupling increases, ranging from the RPA value for $u = 0$, to zero at the onset of the Mott transition. This can be qualitatively understood by considering the classical expression for the plasma frequency, $\omega_p = \sqrt{4\pi n e^2/m^*}$, with n the electron density, e the electron charge, and m^* its effective mass. Recalling that, for an unscreened Coulomb interaction $V = e^2$, and that the band mass is given by the renormalization factor via $z_0^2 t \sim 1/m^*$, we see that the plasma frequency should decrease along with z_0^2 when the Hubbard coupling is increased. This is better depicted in Fig. 3(b), in which ω_p^2 is shown as a function of the renormalization factor (or quasiparticle residue) z_0^2. We clearly see that at the onset of the metal-to-insulator transition, at which the effective mass diverges, ω_p drops to zero. This vanishing of the plasma frequency at the onset of the Mott transition re-emphasises the connection between the quasiparticle and collective nature of the plasmon mode.

Summary and conclusion.— In summary, a proof of principle for the suitability of the radial gauge of the KRSB representation to study charge excitation spectra in the full range of correlation regimes, and in the presence of long range interactions, has been given. We evidenced quantitative and qualitative discrepancies between our results and standard RPA. In particular, we emphasized the influence of strong local correlations on the plasmon collective mode, showing the possibility for the plasmon to propagate undamped in broader ranges of wavelengths at strong coupling, and recovering the expected dependence of the plasma frequency on the renormalized mass of the electrons. At the onset of the Mott transition, the plasma frequency is found to vanish along with the quasiparticle residue. Regions of strong hybridization between the plasmon and upper Hubbard band collective modes have also been unraveled. As the computational cost is similar to that of standard RPA, our method, and possible future generalizations, may be employed to refine the incorporation of strong interactions in studies of realistic correlated systems.

Acknowledgements.— The authors gratefully thank Thilo Kopp for insightful discussions. This work was supported by Région Normandie through the ECOH project. Financial support provided by the ANR LISBON (ANR-20-CE05-0022-01) project is gratefully acknowledged.

[1] D. Bohm and D. Pines, A collective description of electron interactions. I. magnetic interactions, Phys. Rev. **82**, 625 (1951).
[2] D. Pines and D. Bohm, A collective description of electron interactions: II. collective vs individual particle aspects of the interactions, Phys. Rev. **85**, 338 (1952).
[3] D. Bohm and D. Pines, A collective description of electron interactions: III. coulomb interactions in a degenerate electron gas, Phys. Rev. **92**, 609 (1953).
[4] P. W. Anderson, *Basic Notions of Condensed Matter Physics* (Addison-Wesley, Redwood City, CA, 1994).
[5] J. R. Schrieffer, *Theory of Superconductivity* (Frontiers in Physics, Addison-Wesley, New York, NY, 1964).
[6] G. Giuliani and G. Vignale, *Quantum Theory of the Electron Liquid* (Cambridge University Press, 2005).
[7] W. Yan and N. A. Mortensen, Nonclassical effects in plasmonics: An energy perspective to quantify nonclassical effects, Phys. Rev. B **93**, 115439 (2016).
[8] D. E. Chang, A. S. Sørensen, E. A. Demler, and M. D. Lukin, A single-photon transistor using nanoscale surface plasmons, Nat. Phys. **3**, 807 (2007).
[9] H. J. Lezec, J. A. Dionne, and H. A. Atwater, Negative refraction at visible frequencies, Science **316**, 430 (2007).
[10] A. V. Akimov, A. Mukherjee, C. L. Yu, D. E. Chang, A. S. Zibrov, P. R. Hemmer, H. Park, and M. D. Lukin, Generation of single optical plasmons in metallic nanowires coupled to quantum dots, Nature **450**, 402 (2007).
[11] M. A. Noginov, G. Zhu, A. M. Belgrave, R. Bakker, V. M. Shalaev, E. E. Narimanov, S. Stout, E. Herz, T. Suteewong, and U. Wiesner, Demonstration of a spaser-based nanolaser, Nature **460**, 1110 (2009).
[12] R. F. Oulton, V. J. Sorger, T. Zentgraf, R.-M. Ma, C. Gladden, L. Dai, G. Bartal, and X. Zhang, Plasmon lasers at deep subwavelength scale, Nature **461**, 629 (2009).
[13] W. Cai, J. S. White, and M. L. Brongersma, Compact, high-speed and power-efficient electrooptic plasmonic modulators, Nano Lett. **9**, 4403 (2009).
[14] A. Hryciw, Y. C. Jun, and M. L. Brongersma, Electrifying plasmonics on silicon, Nat. Mater. **9**, 3 (2010).
[15] J. A. Schuller, E. S. Barnard, W. Cai, Y. C. Jun, J. S. White, and M. L. Brongersma, Plasmonics for extreme light concentration and manipulation, Nat. Mater. **9**, 193 (2010).
[16] T. Ergin, N. Stenger, P. Brenner, J. B. Pendry, and M. Wegener, Three-dimensional invisibility cloak at optical wavelengths, Science **328**, 337 (2010).
[17] K. M. Mayer and J. H. Hafner, Localized surface plasmon resonance sensors, Chem. Rev. **111**, 3828 (2011).
[18] A. Boltasseva and H. A. Atwater, Low-loss plasmonic metamaterials, Science **331**, 290 (2011).
[19] C. M. Soukoulis and M. Wegener, Past achievements and future challenges in the development of three-dimensional photonic metamaterials, Nat. Photon. **5**, 523 (2011).
[20] K. C. Y. Huang, M.-K. Seo, T. Sarmiento, Y. Huo, J. S. Harris, and M. L. Brongersma, Electrically driven subwavelength optical nanocircuits, Nat. Photon. **8**, 244 (2014).
[21] A. Baev, P. N. Prasad, H. Ågren, M. Samoć, and M. Wegener, Metaphotonics: An emerging field with opportunities and challenges, Phys. Rep. **594**, 1 (2015).
[22] H. A. Atwater and A. Polman, Plasmonics for improved photovoltaic devices, Nat. Mater. **9**, 205 (2010).
[23] S. Linic, P. Christopher, and D. B. Ingram, Plasmonic-metal nanostructures for efficient conversion of solar to chemical energy, Nat. Mater. **10**, 911 (2011).

[24] W. Hou, W. H. Hung, P. Pavaskar, A. Goeppert, M. Aykol, and S. B. Cronin, Photocatalytic conversion of CO_2 to hydrocarbon fuels via plasmon-enhanced absorption and metallic interband transitions, ACS Catal. **1**, 929 (2011).

[25] J. Lee, S. Mubeen, X. Ji, G. D. Stucky, and M. Moskovits, Plasmonic photoanodes for solar water splitting with visible light, Nano Lett. **12**, 5014 (2012).

[26] S. Mukherjee, F. Libisch, N. Large, O. Neumann, L. V. Brown, J. Cheng, J. B. Lassiter, E. A. Carter, P. Nordlander, and N. J. Halas, Hot electrons do the impossible: Plasmon-induced dissociation of H_2 on Au, Nano Lett. **13**, 240 (2013).

[27] D. O'Neal, L. R. Hirsch, N. J. Halas, J. Payne, and J. L. West, Photo-thermal tumor ablation in mice using near infrared-absorbing nanoparticles, Cancer Lett. **209**, 171 (2004).

[28] Y. Li, C. Jing, L. Zhang, and Y.-T. Long, Resonance scattering particles as biological nanosensors in vitro and in vivo, Chem. Soc. Rev. **41**, 632 (2012).

[29] M. Swierczewska, G. Liu, S. Lee, and X. Chen, High-sensitivity nanosensors for biomarker detection, Chem. Soc. Rev. **41**, 2641 (2012).

[30] C. L. C. Smith, N. Stenger, A. Kristensen, N. A. Mortensen, and S. I. Bozhevolnyi, Gap and channeled plasmons in tapered grooves: a review, Nanoscale **7**, 9355 (2015).

[31] V. P. Chavda, P. C. Balar, L. V. Nalla, R. Bezbaruah, N. R. Gogoi, S. N. R. Gajula, B. Peng, A. S. Meena, J. Conde, and R. Prasad, Conjugated nanoparticles for solid tumor theranostics: Unraveling the interplay of known and unknown factors, ACS Omega **8**, 37654 (2023).

[32] A. M. Lewis and T. C. Berkelbach, Ab initio lifetime and concomitant double-excitation character of plasmons at metallic densities, Phys. Rev. Lett. **122**, 226402 (2019).

[33] P. Li, R. Shi, P. Lin, and X. Ren, First-principles calculations of plasmon excitations in graphene, silicene, and germanene, Phys. Rev. B **107**, 035433 (2023).

[34] C. J. C. Scott and G. H. Booth, Rigorous screened interactions for realistic correlated electron systems, Phys. Rev. Lett. **132**, 076401 (2024).

[35] E. G. C. P. van Loon, H. Hafermann, A. I. Lichtenstein, A. N. Rubtsov, and M. I. Katsnelson, Plasmons in strongly correlated systems: Spectral weight transfer and renormalized dispersion, Phys. Rev. Lett. **113**, 246407 (2014).

[36] H. Hafermann, E. G. C. P. van Loon, M. I. Katsnelson, A. I. Lichtenstein, and O. Parcollet, Collective charge excitations of strongly correlated electrons, vertex corrections, and gauge invariance, Phys. Rev. B **90**, 235105 (2014).

[37] M. Guzzo, G. Lani, F. Sottile, P. Romaniello, M. Gatti, J. J. Kas, J. J. Rehr, M. G. Silly, F. Sirotti, and L. Reining, Valence electron photoemission spectrum of semiconductors: Ab initio description of multiple satellites, Phys. Rev. Lett. **107**, 166401 (2011).

[38] J. S. Zhou, M. Gatti, J. J. Kas, J. J. Rehr, and L. Reining, Cumulant Green's function calculations of plasmon satellites in bulk sodium: Influence of screening and the crystal environment, Phys. Rev. B **97**, 035137 (2018).

[39] P. Cudazzo and L. Reining, Correlation satellites in optical and loss spectra, Phys. Rev. Res. **2**, 012032(R) (2020).

[40] L. Zinni, M. Bejas, H. Yamase, and A. Greco, Low-energy plasmon excitations in infinite-layer nickelates, Phys. Rev. B **107**, 014503 (2023).

[41] G. Kotliar and A. E. Ruckenstein, New functional integral approach to strongly correlated Fermi systems: The Gutzwiller approximation as a saddle point, Phys. Rev. Lett. **57**, 1362 (1986).

[42] M. Deeg, H. Fehske, and H. Büttner, Slave-boson phase diagram of the two-dimensional extended Hubbard model: Influence of electron-phonon coupling, Z. Phys. B **91** (1993).

[43] G. Lhoutellier, R. Frésard, and A. M. Oleś, Fermi-liquid Landau parameters for a nondegenerate band: Spin and charge instabilities in the extended Hubbard model, Phys. Rev. B **91**, 224410 (2015).

[44] D. Riegler, J. Seufert, E. H. da Silva Neto, P. Wölfle, R. Thomale, and M. Klett, Interplay of spin and charge order in the electron-doped cuprates, Phys. Rev. B **108**, 195141 (2023).

[45] L. Philoxene, V. H. Dao, and R. Frésard, Spin and charge modulations of a half-filled extended Hubbard model, Phys. Rev. B **106**, 235131 (2022).

[46] V. H. Dao and R. Frésard, Collective modes in the paramagnetic phase of the Hubbard model, Phys. Rev. B **95**, 165127 (2017).

[47] M. Aichhorn, H. G. Evertz, W. von der Linden, and M. Potthoff, Charge ordering in extended Hubbard models: Variational cluster approach, Phys. Rev. B **70**, 235107 (2004).

[48] B. Davoudi and A.-M. S. Tremblay, Nearest-neighbor repulsion and competing charge and spin order in the extended Hubbard model, Phys. Rev. B **74**, 035113 (2006).

[49] M. Y. Kagan, D. V. Efremov, M. S. Marienko, and V. V. Val'kov, Triplet p-wave superconductivity in the low-density extended Hubbard model with Coulomg repulsion, JETP Lett. **93**, 725 (2011).

[50] T. Ayral, S. Biermann, and P. Werner, Screening and nonlocal correlations in the extended Hubbard model from self-consistent combined *GW* and dynamical mean field theory, Phys. Rev. B **87**, 125149 (2013).

[51] E. G. C. P. van Loon, A. I. Lichtenstein, M. I. Katsnelson, O. Parcollet, and H. Hafermann, Beyond extended dynamical mean-field theory: Dual boson approach to the two-dimensional extended Hubbard model, Phys. Rev. B **90**, 235135 (2014).

[52] K. J. Kapcia, S. Robaszkiewicz, M. Capone, and A. Amaricci, Doping-driven metal-insulator transitions and charge orderings in the extended Hubbard model, Phys. Rev. B **95**, 125112 (2017).

[53] M. Schüler, E. G. C. P. van Loon, M. I. Katsnelson, and T. O. Wehling, First-order metal-insulator transitions in the extended Hubbard model due to self-consistent screening of the effective interaction, Phys. Rev. B **97**, 165135 (2018).

[54] H. Terletska, S. Iskakov, T. Maier, and E. Gull, Dynamical cluster approximation study of electron localization in the extended Hubbard model, Phys. Rev. B **104**, 085129 (2021).

[55] M. Roig, A. T. Rømer, P. J. Hirschfeld, and B. M. Andersen, Revisiting superconductivity in the extended one-band Hubbard model: Pairing via spin and charge fluctuations, Phys. Rev. B **106**, 214530 (2022).

[56] E. Linnér, A. I. Lichtenstein, S. Biermann, and E. A. Stepanov, Multichannel fluctuating field approach to

competing instabilities in interacting electronic systems, Phys. Rev. B **108**, 035143 (2023).
[57] S. Kundu and D. Sénéchal, CDMFT+HFD: an extension of dynamical mean field theory for nonlocal interactions applied to the single band extended Hubbard model (2023), arXiv:2310.16075 [cond-mat.str-el].
[58] R. Frésard and T. Kopp, Slave bosons in radial gauge: the correct functional integral representation and inclusion of non-local interactions, Nucl. Phys. B **594**, 769 (2001).
[59] V. H. Dao and R. Frésard, Combining complex and radial slave boson fields within the Kotliar-Ruckenstein representation of correlated impurities, Ann. Phys. (Berlin) **532**, 1900491 (2020).
[60] V. H. Dao and R. Frésard, Exact functional integration of radial and complex slave-boson fields: thermodynamics and dynamics of the two-site extended Hubbard model (2024), arXiv:2402.05701 [cond-mat.str-el].
[61] T. Jolicoeur and J. C. Le Guillou, Fluctuations beyond the Gutzwiller approximation in the slave-boson approach, Phys. Rev. B **44**, 2403 (1991).
[62] R. Frésard and P. Wölfle, Unified slave boson representation of spin and charge degrees of freedom for strongly correlated Fermi systems, Int. J. Mod. Phys. B **06**, 685 (1992).
[63] Y. Bang, C. Castellani, M. Grilli, G. Kotliar, R. Raimondi, and Z. Wang, Single particle and optical gaps in charge-transfer insulators, Int. J. Mod. Phys. B **06**, 531 (1992).
[64] J. Bünemann, M. Capone, J. Lorenzana, and G. Seibold, Linear-response dynamics from the time-dependent Gutzwiller approximation, New J. Phys. **15**, 053050 (2013).
[65] K. Noatschk, C. Martens, and G. Seibold, Time-dependent Gutzwiller approximation: Theory and applications, J. Supercond. Nov. Mag. **33**, 2389 (2020).
[66] R. Frésard, H. Ouerdane, and T. Kopp, Slave bosons in radial gauge: A bridge between path integral and Hamiltonian language, Nucl. Phys. B **785**, 286 (2007).
[67] D. Vollhardt, P. Wölfle, and P. W. Anderson, Gutzwiller-Hubbard lattice-gas model with variable density: Application to normal liquid ^{3}He, Phys. Rev. B **35**, 6703 (1987).

Supplemental Material for Charge Collective Modes in Correlated Electron Systems: Plasmons Beyond the Random Phase Approximation

Loïc Philoxene, Vu Hung Dao, and Raymond Frésard
Normandie Université, ENSICAEN, UNICAEN, CNRS, CRISMAT, 14000 Caen, France

CONTENTS

DEVIATION OF THE RADIAL KRSB CHARGE SUSCEPTIBILITY FROM RPA

In order to assess for the agreement, or disagreement, between the radial KRSB spectra and the predictions of standard perturbation theory, let us compute the function $f^s(\mathbf{q},\omega)$, defined as

$$f^s(\mathbf{q},\omega) = \frac{1}{\chi_c(\mathbf{q},\omega)} - \frac{1}{\Pi_0(\mathbf{q},\omega)}. \tag{1}$$

Note that this quantity is a wavevector and frequency dependent generalization of the usual Landau parameter $F_0^s = N(E_F) f^s(\mathbf{0},0)$, with $N(E_F)$ the density of states at the Fermi energy. In the weak coupling regime, the real part of this function should be equal to $\frac{U}{2} + V(\mathbf{q})$, which would yield the standard RPA charge susceptibility, and deviation from this value thus give a measure of the deviation of the radial KRSB results from perturbation theory.

As can be seen in Fig. 1(a), in which this deviation is displayed, for $V = 0.1\ U$, with $U = 0.01\ U_c$, the radial KRSB results agree with standard perturbation theory in the weak coupling regime. Indeed, we find $\mathrm{Re}\, f^s(\mathbf{q},\omega) \simeq \frac{U}{2} + V(\mathbf{q})$, with deviations of at most 1.5%, irrespective of the energy and wavevector, except in a narrow band around $\omega = U_c/2$. There, deviations of up to 115% are observed. For reasons discussed in the main text, we assign this band to a signature of the upper Hubbard band (UHB), and note that strong deviations around this UHB mode are to be expected, as it is not captured by standard perturbative expansions. As the Hubbard coupling is increased, we observe in Fig. 1(b) and Fig. 1(c) that deviations from $\mathrm{Re}\, f^s(\mathbf{q},\omega) \simeq \frac{U}{2} + V(\mathbf{q})$ away from $\mathbf{q} = \Gamma$ grow, jointly with the deviations around the UHB mode. In particular, we find deviations of up to 15% for $U = 0.10\ U_c$, and 60% for $U = 0.30\ U_c$, outside of the UHB. Additionally the dispersion of the latter is also seen to increase, due to the larger values of $U = 0.10\ U_c$ and $0.30\ U_c$ in Fig. 1(b) and Fig. 1(c), respectively.

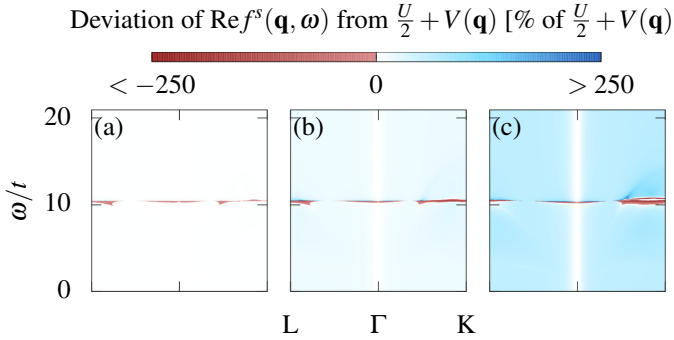

FIG. 1. Deviation of $\mathrm{Re}\, f^s(\mathbf{q},\omega)$ from $\frac{U}{2} + V(\mathbf{q})$. Parameters: $T = 0$, and $V = 0.1\ U$ with (a) $U = 0.01\ U_c$, (b) $U = 0.10\ U_c$ and (c) $U = 0.30\ U_c$.

PLASMA FREQUENCY ON A LATTICE IN THE WEAK COUPLING REGIME

The dispersion $\omega_{\mathrm{plasmon}}(\mathbf{q})$ of the plasmon collective mode is obtained as a solution of

$$\varepsilon(\mathbf{q}, \omega_{\mathrm{plasmon}}(\mathbf{q})) = 0. \tag{2}$$

In the weak coupling regime $U \ll U_c$ and $V \ll U_c$, an analytical expression for the leading contributions to the plasmon dispersion may be obtained by noting that the radial KRSB dielectric function reduces to an RPA form

$$\varepsilon(\mathbf{q},\omega) \simeq 1 + \left[\frac{U}{2} + V(\mathbf{q})\right] \Pi_0(\mathbf{q},\omega). \tag{3}$$

For our purpose, we expand the Lindhard function to lowest order in $\mathbf{q}^2$ about $\mathbf{q} = \Gamma$. Re-writing it as

$$\begin{aligned}\Pi_0(\mathbf{q},\omega) &= \frac{2}{L}\sum_{\mathbf{k}} \frac{f_F(E_{\mathbf{k}+\mathbf{q}}) - f_F(E_{\mathbf{k}})}{\omega - (E_{\mathbf{k}+\mathbf{q}} - E_{\mathbf{k}})} \\ &= \frac{2}{L}\sum_{\mathbf{k}} f_F(E_{\mathbf{k}}) \frac{2E_{\mathbf{k}} - E_{\mathbf{k}+\mathbf{q}} - E_{\mathbf{k}-\mathbf{q}}}{\omega^2 + \omega(E_{\mathbf{k}-\mathbf{q}} - E_{\mathbf{k}+\mathbf{q}}) + (E_{\mathbf{k}+\mathbf{q}} - E_{\mathbf{k}})(E_{\mathbf{k}} - E_{\mathbf{k}-\mathbf{q}})},\end{aligned} \tag{4}$$

then expanding the dispersion as $E_{\mathbf{k}\pm\mathbf{q}} = E_{\mathbf{k}} \pm \mathbf{q}^{\mathrm{T}}\nabla_{\mathbf{k}}E_{\mathbf{k}} + \frac{1}{2}\mathbf{q}^{\mathrm{T}}\mathbf{H}(E_{\mathbf{k}})\mathbf{q} + O(q^3)$, with $\mathbf{H}(E_{\mathbf{k}})$ the Hessian matrix $H_{ab}(E_{\mathbf{k}}) = \partial^2 E_{\mathbf{k}}/\partial k_a \partial k_b$, and using $\omega \gg |\mathbf{q}| \equiv q$ (since ω_p remains finite for finite V), we find

$$\Pi_0(\mathbf{q},\omega) \simeq -\frac{2}{L}\sum_{\mathbf{k}} f_F(E_{\mathbf{k}})\frac{\mathbf{q}^{\mathrm{T}}\mathbf{H}(E_{\mathbf{k}})\mathbf{q}}{\omega^2}. \tag{5}$$

We can moreover make use of the fact that the off-diagonal matrix elements of the Hessian are odd with respect to the components of $\mathbf{k}$, as well as the invariance of the remaining integrals under permutations of the indices of $\mathbf{H}$, such that we end up with the simple form

$$\begin{aligned}\Pi_0(\mathbf{q},\omega) &= -\frac{2}{L}\sum_{\mathbf{k}} f_F(E_{\mathbf{k}})\frac{\sum_a q_a^2 H_{aa}(E_{\mathbf{k}})}{\omega^2} \\ &= -\frac{q^2}{\omega^2}\frac{2}{L}\sum_{\mathbf{k}} f_F(E_{\mathbf{k}})\; t\cos\frac{k_x}{2}\left(\cos\frac{k_y}{2}+\cos\frac{k_z}{2}\right) \\ &= \frac{q^2}{\omega^2}\frac{\xi_{\mathbf{0}}}{6}.\end{aligned} \tag{6}$$

Inserting this expression into Eq. (3), we finally find

$$\omega^2_{\mathrm{plasmon}}(\mathbf{q}) \simeq \omega_p^2\left(1+\frac{\kappa}{\omega_p^2}q^2\right), \tag{7}$$

with

$$\omega_p^2 = -\frac{V\xi_{\mathbf{0}}}{6}, \tag{8}$$

and

$$\kappa = -\frac{U\xi_{\mathbf{0}}}{12}. \tag{9}$$

V is hence pivotal to the very existence of the plasmon altogether, while U rather governs its dispersion. Moreover, both ω_p and κ are sensitive to the lattice on which the electrons evolve through the $-\xi_{\mathbf{0}}/6$ factor. Finally, recalling that in free space $V \sim e^2$, and that the kinetic energy is proportional to the inverse band mass via $t \sim 1/m^*$, we may thus rewrite $\xi_{\mathbf{0}} \sim -6\;\rho/m^*$, with

$$\rho = \frac{2}{L}\sum_{\mathbf{k}} f_F(E_{\mathbf{k}})\cos\frac{k_x}{2}\left(\cos\frac{k_y}{2}+\cos\frac{k_z}{2}\right). \tag{10}$$

The plasma frequency is then recast as

$$\omega_p \sim \sqrt{\frac{e^2\rho}{m^*}}. \tag{11}$$

Up to a factor of 4π, this is the classical expression, apart from the fact that the electron density n has been replaced by ρ. The difference stems from the way we represent the density distribution on the lattice. In contrast to the Fermi gas, for which a homogeneous electron density is given by a continuous (constant in this case) function of the position, we here deal with a discretized and periodic function of the position $\mathbf{R}$: $n(\mathbf{R}) \sim \sum_j \delta(\mathbf{R}-\mathbf{r}_j)$, where $\mathbf{r}_j$ is a lattice vector. The Coulomb potential then couples to this set of discrete and periodic lattice bonds, and taking its Fourier transform results in contributions from the lattice harmonics. Therefore, the lattice-dependent ρ appears in the plasma frequency instead of $n = 2\int \frac{\mathrm{d}^3\mathbf{k}}{(2\pi)^3} f_F(\frac{k^2}{2m^*})$ for the Fermi gas.